buildings

Article

Numerical Study on Welding Residual Stress and Microstructure in Gas Metal Arc Welding Square Tube–Plate Y-Shaped Joints

Zhaoru Yan [1] and Jinsan Ju [2,*]

[1] School of Mechanics and Civil Engineering, China University of Mining and Technology—Beijing, Beijing 100083, China; yzr@student.cumtb.edu.cn
[2] College of Water Resources and Civil Engineering, China Agricultural University, Beijing 100083, China
* Correspondence: jujinsan@cau.edu.cn

Abstract: Welding residual stresses significantly influence the mechanical behavior of hollow section joints, especially in the pivotal connection zones of steel structures employed in construction. The research object of this study is the Q355 steel square tube–plate Y-joint welded using Gas Metal Arc Welding (GMAW) with CO_2 Shielding. The thermodynamic sequence coupling method was employed to simulate the temperature field, microstructure distribution, and welding residual stresses in square tube–plate Y-joints. Based on the monitored temperature field data and the cross-sectional dimensions of the weld pool, this study calibrated the finite element model. Subsequently, the calibrated finite element model was employed to analyze the influence of microstructural phase transformations and welding sequences on the welding residual stresses in square tube–plate Y-joints. The research findings indicate that the peak transverse welding residual stresses in the branch pipes of the four joint zones were lower when considering the phase transformation effect than when not accounting for it in the calculations. There was no significant difference in the transverse and longitudinal welding residual stresses on the surface of branch pipes under the three welding sequences. However, there were certain differences in the microstructural content of the weld zones under the three welding sequences, with the martensite content in the third welding sequence being significantly lower than that in the other two sequences.

Keywords: square tube–plate joint; multi-layer and multi-pass welding; phase transformation microstructure; numerical simulation; welding residual stress

Citation: Yan, Z.; Ju, J. Numerical Study on Welding Residual Stress and Microstructure in Gas Metal Arc Welding Square Tube–Plate Y-Shaped Joints. *Buildings* **2024**, *14*, 3686. https://doi.org/10.3390/buildings14113686

Academic Editor: Mizan Ahmed

Received: 30 October 2024
Revised: 14 November 2024
Accepted: 18 November 2024
Published: 19 November 2024

1. Introduction

Welded connections are the primary means in hollow-section structures. The main advantages of welded connections include their simplicity in detail, material conservation, ease of fabrication, and good sealing performance; moreover, welded connections do not weaken the cross-sectional area of members. However, the welding process also has its drawbacks, such as the negative impact of welding-induced residual stresses and deformations on the mechanical properties of the structure, as well as the prominent issue of low-temperature embrittlement in welded structures. In steel structures, welding residual stress can reduce the bearing capacity [1–3] and fatigue strength [4–6]. Therefore, predicting welding residual stress and deformation is crucial for the safety assessments of steel pipe structures.

In the analysis of welding residual stress and deformation, the accurate calculation of the transient temperature field of the weldment during the welding process plays a pivotal role. Numerical simulation of the welding temperature field depends primarily on the heat source model, heat dissipation conditions, material properties, and welding parameters. The heat source model represents the distribution of welding heat energy on the workpiece and serves as the foundation for temperature field analysis. Volumetric heat source models are commonly used, including hemispherical, ellipsoidal, and double-ellipsoidal heat sources [7,8]. In simulations, the heat source model type is determined based on the welding method, and the heat source parameters are adjusted to match the actual weld cross-sectional dimensions. This ensures that the size parameters of the heat source model align with the actual weld pool cross-section [9–11]. Wang et al. [12], Cui et al. [13], and Ji et al. [14] found that the arc heat power and welding speed significantly affect the temperature field peak, size of the weld pool, and dimensions of the heat-affected region, which subsequently affect the mechanical and microstructural properties of the welded joint. Studies by Cheon et al. [15] and Zhang et al. [16] indicate that stress and phase transformation have relatively weak effects on the temperature field, while the welding temperature field controls the phase transformation and stress–strain field changes in metal structures.

Utilizing the advanced finite element simulation techniques, researchers have embarked on a more profound investigation into the residual stress present in joints of low-alloy high-strength steel. Malik et al. [17] introduced a computational method for analyzing the temperature distribution and residual stress fields in the arc welding process of low-carbon steel thin-walled cylinders. The influence of key welding process parameters on welding residual stresses was investigated through parameterized studies based on numerical simulations. Joshi et al. [18] conducted a study on the welding residual stresses of Circular Hollow Section (CHS) T-joints using the finite element simulation techniques. They obtained the distribution of the residual stresses in different directions at the joint. Kimiya et al. [19] utilized numerical simulation methods to analyze the welding residual stress field of S355 structural steel circular pipe butt joints and compared this with experimental results to confirm the reliability and accuracy of the numerical model. Gadallah et al. [20] employed an efficient numerical analysis approach based on the finite element method to investigate the influence of welding residual stresses on the mixed-mode stress intensity factors of non-planar surface cracks in tubular T-joints with a rounded weld toe. Deng et al. [21] analyzed the impact of welding on the strength and stiffness of Y- and K-shaped joints in steel–concrete composite columns by numerical simulation methods. Wang et al. [22] examined the effects of the welding sequence on the distribution of residual stress and deformation in Q345 H-shaped steel welded joints using a combination of numerical simulation and experimental methods. Zhang et al. [23] analyzed the effects of different welding construction processes on the temperature field and residual stresses of Q355 steel corrugated web plates. He et al. [24] investigated the effects of the groove angle on the thermal temperature history, residual stresses, and welding deformation of Q355/316L dissimilar welded steel joints with an 8 mm medium-thick plate using experimental and numerical simulation methods. Akduman et al. [25] investigated the post-fire performance of beam–column end plate bolted connections with various geometric properties using numerical simulation and experimental methods. The findings revealed that high temperatures lead to a decrease in the load-bearing capacity at the connection points.

The aforementioned research did not consider the influence of microstructural transformations on the residual stresses and deformation in welding. Metal structures undergo complex solid-state phase transformations during the welding process, including diffusion-induced (ferrite, pearlite, and bainite) and non-diffusion-induced (martensite) phase transformations. However, obtaining specific details of the phase transformations occurring in the weld joint during welding can be challenging using purely experimental methods. The continuous development of computer simulation technology has provided strong theoretical support for solving these issues. The Johnson–Mehl–Avrami–Kolmogorov (JMAK) equation is widely used for modeling phase transformations induced using diffusion [26]. It is crucial to determine the parameters K and n, which can be obtained from the Time–Temperature–Transformation (TTT) curve [27–29]. Additionally, these parameters can be obtained from Continuous Cooling Transformation (CCT) diagrams [30], which enhance the versatility of the JMAK equation. Deng and Murakawa [31] derived the parameters K and n from the CCT diagram of 2.25Cr-1Mo steel and applied the JMAK equation to determine the volume fraction of bainite in welded joints. Hu et al. [32] utilized Abaqus software to analyze the temperature field, microstructure distribution, and hardness distribution of Q345 steel plate weld joints. They investigated the suitability and precision of the JMAK equation obtained from various CCT diagrams for predicting the microstructures of welded joints. Based on the JMAK equation, Li et al. [33] established a predictive model for the welding process of Ti-6Al-4V titanium alloy using the finite element method. This model was employed to evaluate the phase composition, residual stresses, and deformation of Ti-6Al-4V sheet weld joints under various welding techniques. To perform the calculation of non-diffusion-induced phase transformations, most researchers have used the Koistinen–Marburger (K-M) equation. Esfahani et al. [34] employed a finite element model to simulate the temperature gradients, phase volume fractions, stress variations, and dimensional changes in 1045 cylindrical hypoeutectoid steel samples during quenching, which were then validated against experimental measurements. Wei et al. [35] developed a multi-physics coupled numerical model to investigate the martensitic phase transformation kinetics during deep cryogenic treatment. Sun et al. [36] used the finite element method to simulate the temperature field, phase field, and stress–strain field of face-hobbed hypoid gears throughout various heat treatment processes and verified the accuracy of the phase transition structure and deformation through experiments.

Based on previous research, it is evident that welding studies on hollow section joints have mainly concentrated on the interaction between temperature and stress fields, neglecting the impact of microstructure changes on residual welding stresses. Furthermore, there is a lack of research on the welding of square tube–plate joints. Therefore, this study aims to comprehensively investigate the coupling between temperature, phase transformation, and stress in the welding of Q355 steel square tube–plate Y-shaped joints using numerical simulation methods. In Section 2, temperature monitoring instruments are employed to monitor the welding temperature field of a test joint throughout the entire welding process, acquiring temperature–time curves for different joint regions. In Section 3, this study focuses on the simulation calculation process and the corresponding theoretical foundation for the temperature-phase transformation–stress coupling issue in the welding of square tube–plate joints. In Section 4, this study calculates the temperature field of square tube–plate Y-joints. The numerical simulation results of the temperature field are compared with experimental measurements to verify the accuracy of the finite element method. In Section 5, this study analyzes the influence of microstructural transformations in various regions of the joints on the welding residual stresses in these areas. Furthermore, it investigates the residual stresses on the surface of branch pipes in different joint regions under three welding sequences, as well as the microstructural content of welds in these zones.

2. Welding Temperature Field Monitoring of the Square Tube–Plate Y-Shaped Joint

2.1. Design and Material of the Square Tube–Plate Y-Shaped Joint

The base material of the square tube–plate Y-joint is Q355 steel, and its chemical composition is shown in Table 1. The chemical composition was measured using a SPECTROMAXx device (SPECTRO Analytical Instruments, Kleve, Germany). The angle θ between the axis of the branch pipe and the rigid plate was 60°. The length h_i and width b_i of the branch pipe section of the joint were both 200 mm and the thickness t_i was 10 mm. The length h_0, width b_0, and thickness t_0 of the joint plate were 500 mm, 300 mm, and 16 mm, respectively. A physical diagram of the joint is shown in Figure 1.

Table 1. Chemical composition of the base and weld metals (% weight).

Chemical Composition	C	Si	Mn	Cr	Ni
Base metal (Q355)	0.17	0.02	1.6	0.03	0.02
Weld metal (T492T1-1C1A)	0.055	0.37	1.52	0.042	0.02

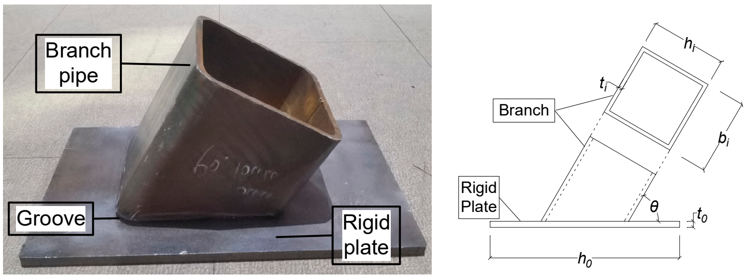

Figure 1. Physical and dimensional schematic diagram of the square tube–plate Y-joint.

2.2. Welding and Temperature Monitoring Process

Before welding the square tube–plate Y-shaped joint, the four edges of the branch pipe were beveled, with the angle of the single V groove α set to 60°. The steel plate is positioned atop the support platform without securing, whereas the branch pipe is affixed at its four corner points by means of welding to the steel plate. A combination of butt and fillet welds was used to connect the branch pipe to the steel plate. The welding method for the joint employed GMAW with CO_2 Shielding. The welding material used was a 1.2 mm diameter T492T1-1C1A wire (Tianjin Jinqiao Welding Materials Group Co., Ltd., Tianjin, China). The chemical composition of the welding material was measured using the SPECTROMAXx device, and the results are presented in Table 1. The welding process utilized a KRII-500 welding machine (Shandong Aotai Electric Co., Ltd., Jinan, China), maintaining a CO_2 gas flow rate of 20~25 L/min.

As shown in Figure 2, a method using two layers and three passes of welding seams was adopted in regions A (the toe of the joint), B (on the side), and D (at the root). The three weld passes were numbered WP-1, WP-2, and WP-3. The welding sequence was as follows: region A, region B1, region D, region B2. By repeating this welding sequence three times, the length of the welding leg h_l was 1.5 times that of t_i. A layout diagram of the detection points on the tubular joint is shown in Figure 3. The temperature detection points were set on the four outer surfaces of the branch pipes, at 40 mm, 70 mm, and 100 mm from the weld seam. Furthermore, the spacing between detection points was at least 50 mm. A total of 25 detection points were installed in the tubular joint. The current I, voltage U, welding time, and welding speed during the welding process of the tubular joint are listed in Table 2. The equipment used to monitor the temperature during the welding process was an Anbai-AT4732 device (Changzhou Applent Instruments Ltd., Changzhou, China), which simultaneously collected and recorded temperature fluctuations at 32 points with a fast response time and consistent data stability. The temperature detection range of the thermocouple was −200 °C to 1350 °C.

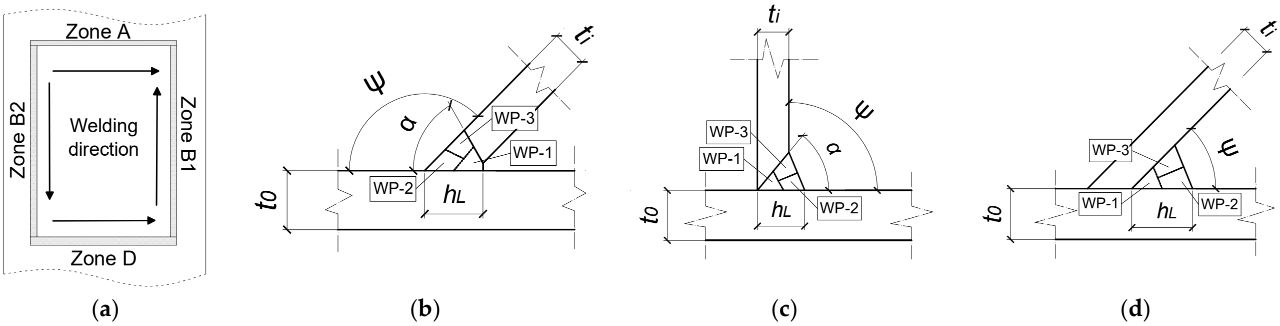

Figure 2. Schematic diagram of the tubular joint welding process (**a**); The appearance of welds in Zone A (**b**); The appearance of welds in Zone B1 and B2 (**c**); The appearance of welds in Zone D (**d**); (Ψ: dihedral angle).

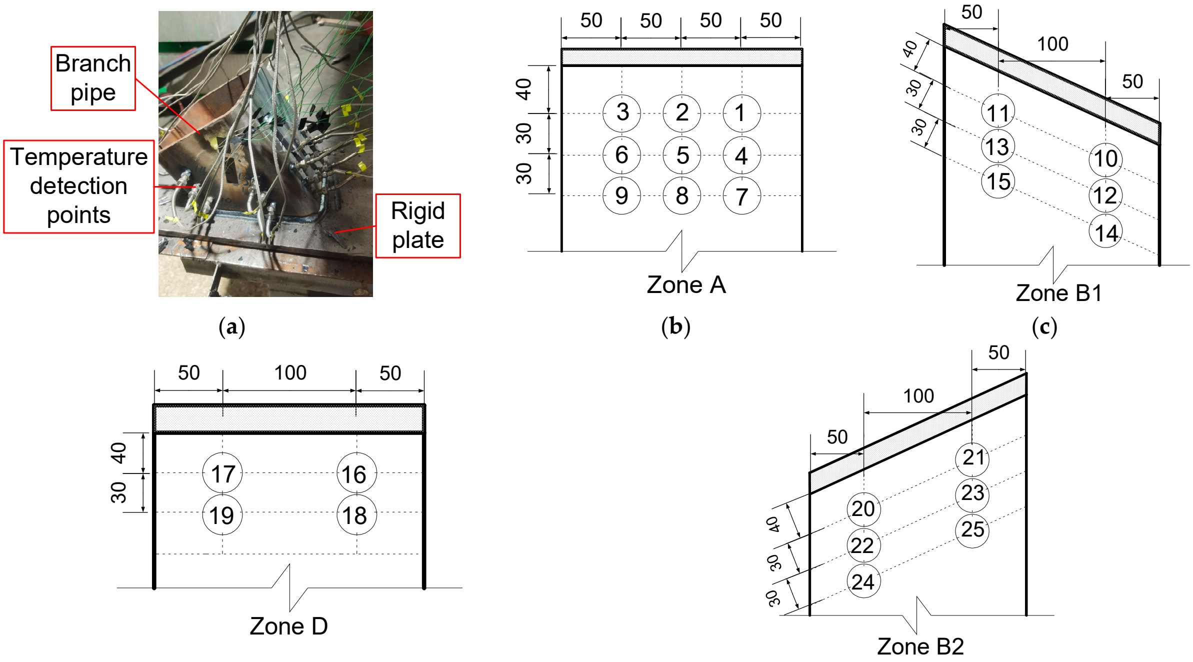

(**a**) (**b**) (**c**)

(**d**) (**e**)

Figure 3. Layout diagram of the temperature detection points for the tubular joint: On-site temperature field monitoring (**a**); Zone A (**b**); Zone B1 (**c**); Zone D (**d**); Zone B2 (**e**).

Table 2. Parametric statistics results of the welding process of the square tube–plate Y-shaped joint.

Weld Pass No.	Current I (A)	Voltage U (V)	Weld Time t (s)	Welding Speed v (mm/s)	Cooling Time t (s)
01	150	30	198	4.35	240
02	210	30	177	4.86	160
03	160	30	145	5.94	/

2.3. Results

The temperature field monitoring results for the branch pipe at the joint are displayed in Figure 4a–c. Figure 4a illustrates the temperature fluctuations on the branch pipe surface over time, 40 mm from the weld seam. It is evident that the temperature increased from ambient conditions to 74 °C during the first weld pass, then decreased to 61 °C; during the second weld pass, it rose gradually from 61 °C to 116 °C, followed by a decrease to 97 °C; and during the third weld pass, it increased from 97 °C to 139 °C before returning to ambient conditions.

Figure 4b shows the temperature variations on the branch pipe surface over time, 70 mm from the weld seam. It can be noted that the temperature progressively increased from ambient conditions to 76 °C from the first weld pass to the end of the third weld pass, and then it returned to ambient conditions. In Figure 4c, the temperature changes on the branch pipe surface over time, 100 mm from the weld seam, are depicted. It can be observed that the temperature gradually rose from ambient conditions to 61 °C from the first weld pass to the end of the third weld pass, and then it decreased back to ambient conditions.

The peak temperature values at different monitoring points after each weld pass were also analyzed. These values were organized by the average temperature peak distance using the weld seam position curve (Figure 4d), depending on their proximity to the weld seam. The data indicated that the peak temperature of the branch pipe decreased as the distance from the weld seam increased. Furthermore, the peak temperature increased with the number of weld passes.

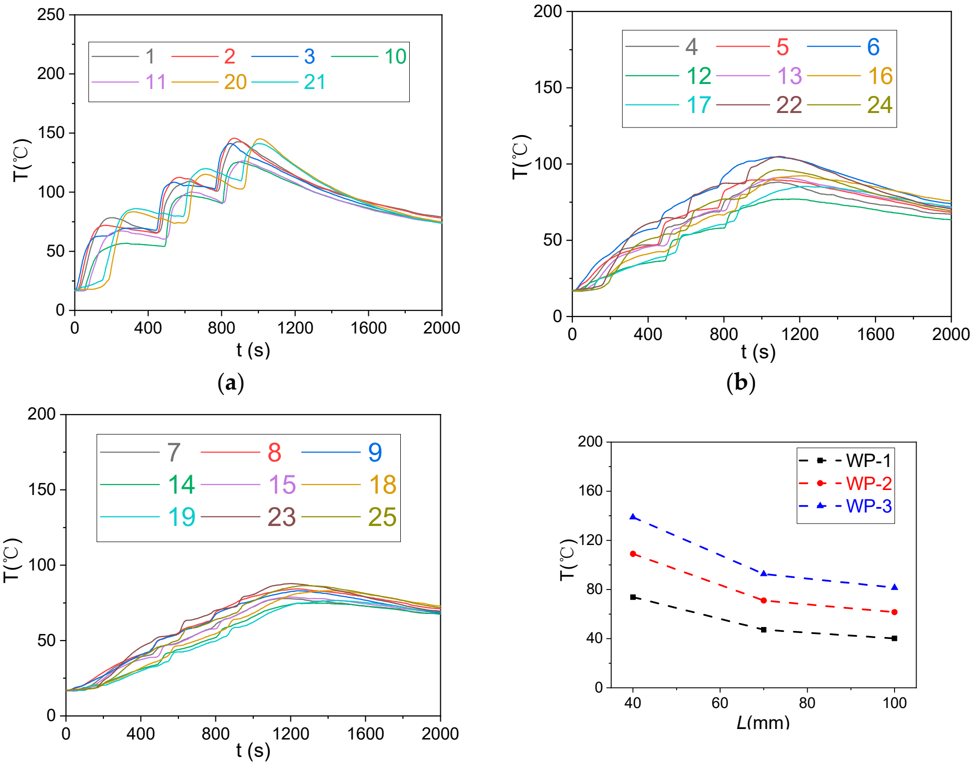

(**a**) (**b**) (**c**) (**d**)

Figure 4. (**a**) The temperature-time curve at a location 40 mm from the weld on the surface of the branch pipe; (**b**) The temperature-time curve at a location 70 mm from the weld on the surface of the branch pipe; (**c**) The temperature-time curve at a location 100 mm from the weld on the surface of the branch pipe; (**d**) The average maximum temperature at different positions from the weld seam at the completion time of each weld pass. (T represents temperature, t represents time, L represents distance).

3. Numerical Simulation of the Square Tube–Plate Y-Shaped Joint Welding

3.1. Finite Element Model of the Square Tube–Plate Y-Shaped Joint

Welding is an intricate metallurgical process, particularly regarding the thermodynamic properties and phase transformation parameters of the materials used. Thus, in this study, the material parameters for Q355 steel and T492T1-1C1A welding filler materials were determined using JmatPro 7.0 software [37]. The detailed thermodynamic properties, microstructure phase transformation material parameters, and TTT curves are illustrated in Figure 5. The obtained material parameters were imported into the Simufact Welding 2020 software [38] to calculate the welding temperature field, microstructure composition, and residual stress of the multi-layer and multi-pass welded Y-shaped square tube–plate joint. The calculation process fully considered the thermo-elastic–plastic constitutive relationship, phase transformation, moving heat source, and boundary conditions of the Q355 base material and welding filler. The intricate details of this calculation process are illustrated in Figure 6a. The three-dimensional modeling of the branch pipe and steel plate was conducted in accordance with the precise dimensions of the joint as specified in Section 2.1.

In establishing the model's boundary conditions, this study considers the vertical support force exerted by the supporting platform on the steel plate, as well as the gravitational loads imposed by the steel plate and the branch pipe themselves. The weld region of the joint had a large heat distribution gradient. Selecting the appropriate grid sizes and element types ensured calculation accuracy and efficiency. A sensitivity analysis of the mesh size reported in [20,23] indicates that within a mesh size of 2.0 mm in the joint welding area, there is no significant difference in the surface temperature and residual stress of the joint. Therefore, the mesh size in the welding area of the joint is set to approximately 2.0 mm, while the mesh size away from the welding area is one-third of the wall thickness of the branch pipe and steel plate. The eight-node hexahedral element is used for both the joint base metal and the weld seam, which is consistent with [20,23]. The mesh division and welding assembly of the Y-shaped square tube–plate joint are depicted in Figure 6b.

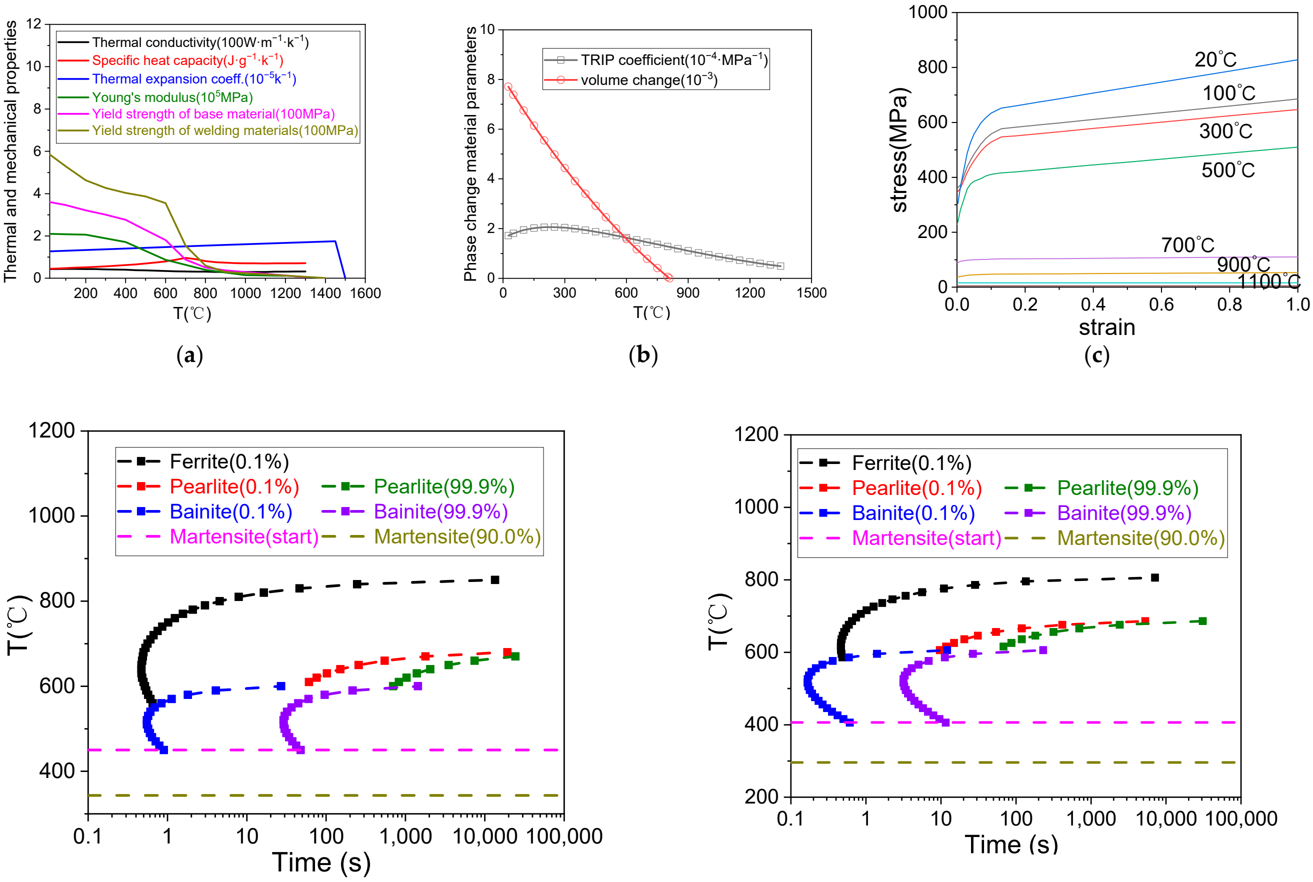

(**a**) (**b**) (**c**)

(**d**) (**e**)

Figure 5. (**a**) Thermodynamic performance parameters of the square-tube joint; (**b**) Phase transformation material parameters; (**c**) The stress–strain curves of the base material at different temperatures; (**d**) TTT curves of the deposited metal; and (**e**) TTT curves of the base material. (T represents temperature).

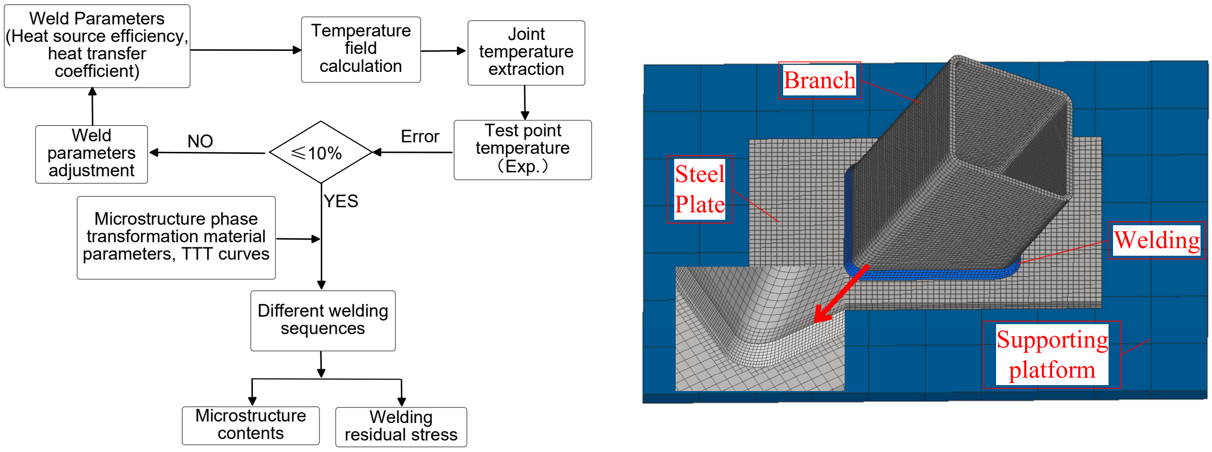

(**a**) (**b**)

Figure 6. The calculation process for the temperature field, residual stress, and microstructure content at the joint (**a**); Schematic of the welding assembly and mesh division (**b**).

3.2. Numerical Simulation of the Temperature Field

During the welding process, the temperature field changed with the movement of the heat source center. Therefore, the temperature exhibited a nonlinear distribution, and the temperature at each joint followed the following heat conduction equation [16]:

$$\rho c\frac{\partial T}{\partial t} = \frac{\partial}{\partial x}(\lambda\frac{\partial T}{\partial x})+\frac{\partial}{\partial y}(\lambda\frac{\partial T}{\partial y})+\frac{\partial}{\partial z}(\lambda\frac{\partial T}{\partial z}) + Q_c \tag{1}$$

where ρ is the material density, c is the specific heat capacity, λ is thermal conductivity, T is temperature, and Q_c is the intensity of the internal heat source.

The most representative spherical heat source model is the Double-Ellipsoidal Heat Source Model proposed by Goldak [7], which is widely used in simulations of welding temperature fields. As shown in Figure 7, along the welding direction, the Double-Ellipsoidal Heat Source Model is divided into two parts, namely, q_1 and q_2. The heat flux density at any point (x, y, and z) inside the heat source is expressed as follows:

$$q_1(\mathrm{x},\mathrm{y},\mathrm{z}) = \frac{6\sqrt{3}Qf_1}{\pi\sqrt{\pi}a_1bc}\exp[-3(\frac{\mathrm{x}^2}{a_1^2}+\frac{\mathrm{y}^2}{b^2}+\frac{\mathrm{z}^2}{c^2})] \tag{2}$$

$$q_2(\mathrm{x},\mathrm{y},\mathrm{z}) = \frac{6\sqrt{3}Qf_2}{\pi\sqrt{\pi}a_2bc}\exp[-3(\frac{\mathrm{x}^2}{a_2^2}+\frac{\mathrm{y}^2}{b^2}+\frac{\mathrm{z}^2}{c^2})] \tag{3}$$

$$f_1+f_2=2,\ Q=\eta UI \tag{4}$$

where q_1 and q_2 represent the distribution coefficient of the heat flow volume of the front and rear ellipsoid, respectively. Moreover, a_1, a_2, b, and c represent the volume distribution parameters of the heat source. Q represents the actual heat input, and η represents the actual heat input. The arc efficiency of the adopted carbon dioxide arc welding was 0.8 [20–23]. U represents the arc voltage and I represents the arc current. Additionally, f_1 and f_2 represent the heat distribution coefficient of the front and rear ellipsoid, respectively. The relevant parameters were all set to 1.0 [23]. In this study, the weld pool dimensions, width 2b and depth c, were measured in different joint regions, and the specific values are listed in Table 3. The width 2b and depth c of the weld pool in the numerical simulation were taken as the measured mean values (Figure 8), thus determining the values of a_1 and a_2 in the double ellipsoidal heat source model [11,23]. The parameter values of the double ellipsoidal heat source model at different regions and weld passes of the square tube–plate Y-shaped joint are shown in Table 3, where the values of a_1 and a_2 were between 2.0 mm and 3.5 mm.

Table 3. Statistical results of the weld pool parameters for the square tube–plate Y-shaped joint.

Bead No.	Joint Region	2b (mm)	c (mm)	a_1 (mm)	a_2 (mm)
01	A	8.9	4.8	2.0	3.0
	B	9.3	4.9		
	D	9.1	5.1		
	Mean value	9.1	4.9		
02	A	11.7	6.0	2.0	3.5
	B	12.5	6.3		
	D	11.3	6.4		
	Mean value	11.8	6.2		
03	A	11.5	6.2	2.0	3.5
	B	11.4	6.5		
	D	11.2	6.6		
	Mean value	11.4	6.4		

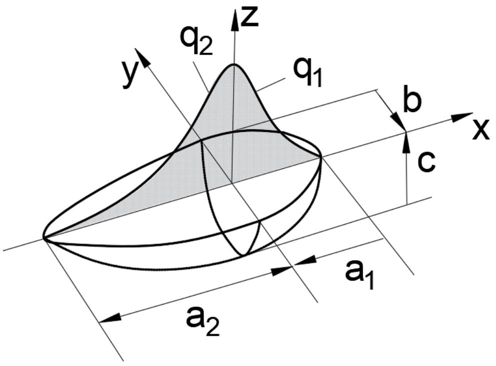

Figure 7. Schematic diagram of size parameters in the Double-Ellipsoidal Heat Source Model.

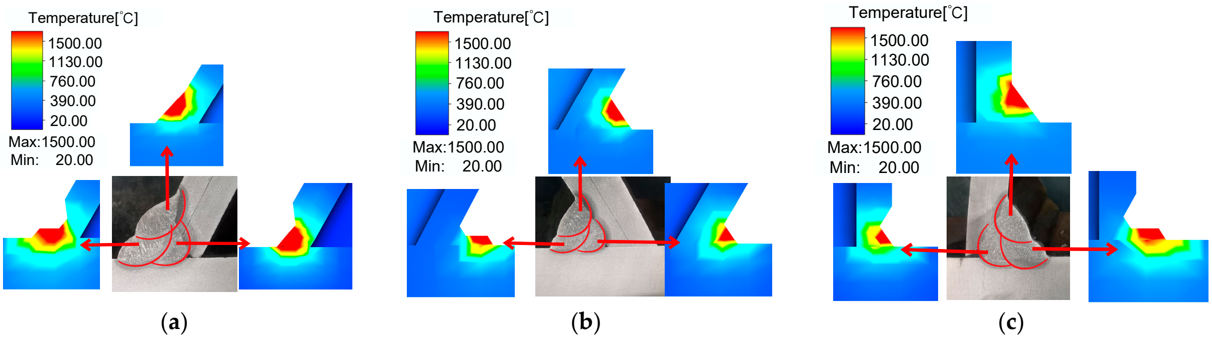

(**a**) (**b**) (**c**)

Figure 8. Comparison of the cross-section test and the numerical simulation of welds in different joint regions and weld passes. (**a**) Region A; (**b**) Region B1 and B2; (**c**) Region D.

In the thermal analysis, the boundary conditions mainly included the convective heat transfer coefficient and thermal radiation between the material surface and air. In engineering practice, a heat-dissipation surface refers to the exposed parts of the base material of tubular joints and each layer of the weld seam. Normally, the heat exchange surface on the weld seam is activated as the welding progresses. In addition, thermal convection was conducted according to Newton's law [32] and following the equation below:

$$q_e = -h_a(T_a - T_b) \tag{5}$$

where q_e represents the heat exchange rate between the weld and the environment, h_a is the convective exchange coefficient, T_a is the surface temperature of the weld, and T_b represents the ambient temperature.

The thermal radiation between the weld and the environment follows Stefan Boltzmann's law [32], as follows:

$$q_f = -\varepsilon\sigma\left[(T_a+273)^4 - (T_b+273)^4\right] \tag{6}$$

where q_f represents the heat loss in the radiation of the welding piece; σ represents the Stefan Boltzmann constant, which is 5.67×10^{-8} w·m^{-2}·°C^{-4}; and ε represents the thermal radiation coefficient.

In the finite element numerical simulations of welding temperature fields, the nonlinear thermal parameters of the material have a significant influence on the calculation results. In this study, the specific heat capacity and thermal conductivity of the austenite, ferrite, pearlite, bainite, and martensite microstructures in the base metal and weld metal of the joint were obtained using the material performance analysis software. Additionally, the latent heat of the metals influenced the welding heat transfer process, with the melting latent heat of the base metal and weld metal being 256.4 J·g^{-1} and the solid–liquid phase line temperatures being 1450 °C and 1500 °C, respectively. The cooling process of the temperature–time curve was significantly influenced by the convective heat transfer coefficient and thermal radiation coefficient. Therefore, in this study, the convective heat transfer coefficient was determined to be $6\mathrm{w}\cdot\mathrm{m}^{-2}\cdot\mathrm{k}^{-1}$ and the thermal radiation coefficient was set to 0.8, based on the cooling rate of the temperature–time curves obtained from the experimental measurement points using a trial-and-error method.

3.3. Calculation of the Microstructure Distribution

During the welding process, the initial phases of the base metal and weld metal underwent austenitization due to heating, whereas the supercooled austenite formed during the post-welding cooling process underwent a transformation through decomposition. Consequently, the calculation of the microstructural distribution was divided into two separate processes. In the welding simulation software, the austenite transformation formula for welding heating was based on a simplified austenite model. This model assumed that when the welding temperature reached Ac3, the phase fraction was 100% austenite.

During the post-welding cooling process, both the base and weld metals underwent diffusion and non-diffusion phase transformations. The JMAK equation [25] was used to describe the isothermal diffusion transformation process of the supercooled austenite as follows:

$$f = 1 - \exp(-Kt^n) \tag{7}$$

where f represents the volume fraction of the phase; T represents the time of the phase transition; and K and n are the material parameters of the dynamic equation, which are related to the temperature, austenite grain size, and chemical composition.

For non-diffusional transformations, such as the formation of martensite from supercooled austenite without atomic diffusion, the K-M equation [39] can be used to calculate the volume fraction of martensite (f_M) as follows:

$$f_M = f_A(1 - \exp(-\alpha(M_S - T))) \quad (T \leqslant M_S) \tag{8}$$

where f_A represents the volume fraction of austenite, M_s represents the temperature at which martensite transformation begins, T represents the temperature during the phase transformation, and α is a material coefficient (typically taken as 0.011).

3.4. Mechanical Performance Analysis of Joints

During the welding process, the thermal and phase transformation strains generated a continuously fluctuating internal stress field. The generation of thermal strain in the welded component was due to large temperature gradients and changes in the thermodynamic properties with temperature. The generation of the phase transformation strain in the welded component was accompanied by the evolution of the microstructure during the solid-state phase transformation, resulting in an additional volumetric strain. Simultaneously, changes in the microstructure also induced plasticity during phase transformation. Therefore, the total strain (ε) can be expressed as the sum of individual components, as follows:

$$\varepsilon = \varepsilon^e + \varepsilon^p + \varepsilon^{th} + \varepsilon^{pt} + \varepsilon^{tr} \tag{9}$$

where ε^e is the elastic strain, ε^p is the plastic strain, ε^{th} is the thermal strain, ε^{pt} is the volume phase transition, and ε^{tr} is the phase transition plastic strain. Reference [39] offers a comprehensive explanation of the formulas for each parameter in Equation (9).

4. Numerical Simulation Results of the Temperature Field

Using the numerical simulation method, temperature–time curves were obtained for different measurement points on the square tube–plate Y-shaped joint in various regions. The temperature–time curves obtained through numerical simulations and experimental measurements were compared, as shown in Figure 9. The solid line represents the temperature–time curve obtained from the experiments and the dashed line represents the values obtained from the numerical simulation. In Figure 9, the temperature at 40 mm from the weld seam fluctuated significantly over time, showing distinct alternating patterns of heating during welding and the subsequent cooling. The temperatures at distances of 70 mm and 100 mm from the weld seam continued to increase until all three weld passes were completed, after which the temperature decreased. The variation pattern of the joint temperature field obtained through the numerical simulation in this study was consistent with the experimentally measured pattern. The average temperature peaks at the measurement points at the same distance from the weld seam were calculated at the end of each weld pass. The averages obtained from the numerical simulations and experimental measurements are listed in Table 4. The comparison results show that the relative errors between the numerical simulation and experimental temperature averages at distances of 40 mm, 70 mm, and 100 mm from the weld seam were within 10%. In summary, this study employed a moving heat source accounting for material nonlinearity. Moreover, the welding parameters and ambient temperature values obtained from the experiments were integrated into the model to accurately simulate the welding temperature field of a Y-shaped intersecting joint under multi-layer and multi-pass welding processes.

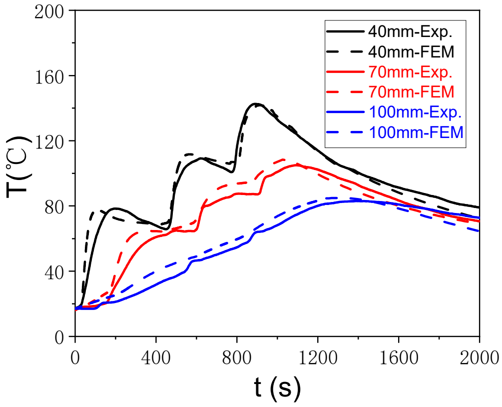

Figure 9. Temperature–time curves at various distances from the weld seam for both experimental and numerical simulation methods. (T represents temperature, t represents time).

Table 4. Comparison of the average peak temperature at different positions at the completion of each weld pass.

Distance to Weld Seam (mm)	**Method**	**Average Temperature at the Completion of Each Weld Pass (°C)**		
		WP-1	**WP-2**	**WP-3**
40	Exp.	73.82	115.98	138.82
	FEM	80.65	121.27	140.55
	Error (%)	9.25	4.56	1.25
70	Exp.	55.24	76.02	92.61
	FEM	58.34	81.76	98.41
	Error (%)	5.61	7.55	6.26
100	Exp.	40.13	61.55	81.50
	FEM	42.73	66.27	86.81
	Error (%)	6.48	7.67	6.52

Note: The formula for calculating relative error was: $|T_{FEM} - T_{Exp.}|/T_{Exp.}$, where T_{FEM} represents the numerical simulation temperature peak and $T_{Exp.}$ represents the experimental temperature peak.

5. Influencing Factor Study

5.1. The Effect of Phase Transformation on the Residual Stresses in Welded Joints

This section focuses on the experimental welding joint in Section 2 as the research subject, analyzing the distribution of residual stress on the surface of the branch pipes in various regions along path "M", with and without considering the phase transformation effects. Figure 10 presents the simulation results without considering the phase transformation. The transverse residual stresses along path "M" were tensile stresses near the weld, which decreased from 330 Mpa to zero as the distance from the weld increased. The longitudinal residual stresses along path "M" were also tensile stresses near the weld, which decreased from 400 Mpa to zero with increasing distance from the weld. Figure 11 presents the simulation results with consideration of the phase transformation. The transverse residual stresses along path "M" were tensile stresses near the weld, which decreased from 270 Mpa to zero as the distance from the weld increased. The longitudinal residual stresses along path "M" were also tensile stresses near the weld, which decreased from 400 Mpa to zero with increasing distance from the weld. These findings align with the research results of Y-shaped joints as reported in [20]. The peak longitudinal residual stresses in the branch pipes near the weld exceeded the peak transverse residual stresses in each region also surpassed the yield strength of the base material of the branch pipes. When the phase transformation effects were considered in the joint, the peak transverse residual stresses near the weld were lower than those for which the phase transformation effects were not considered. Regions A, B1, B2, and D exhibited reductions of 17.41%, 25.81%, 9.45%, and 8.13%, respectively. During the cooling process, the transformation of various microstructures induced volume expansion, offsetting some of the deformation caused by thermal contraction and ultimately reducing welding residual stresses.

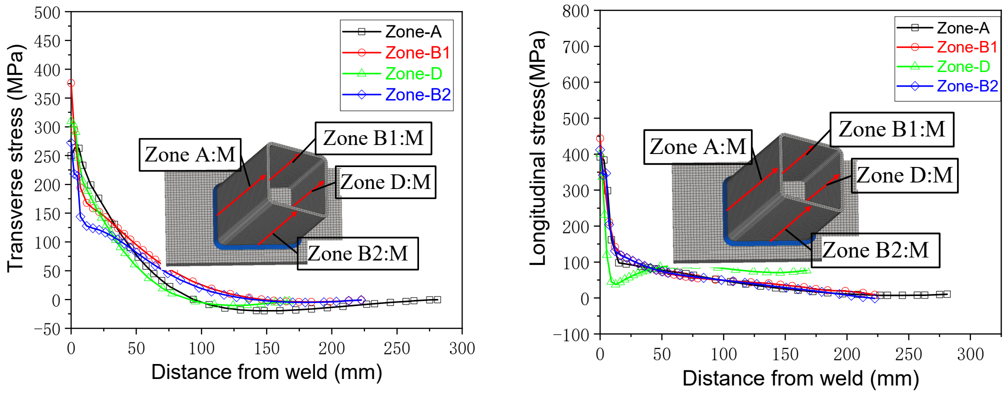

(**a**) (**b**)

Figure 10. Residual stress distribution in the branch pipes of the joint without considering phase transformation effects: (**a**) Transverse; (**b**) Longitudinal.

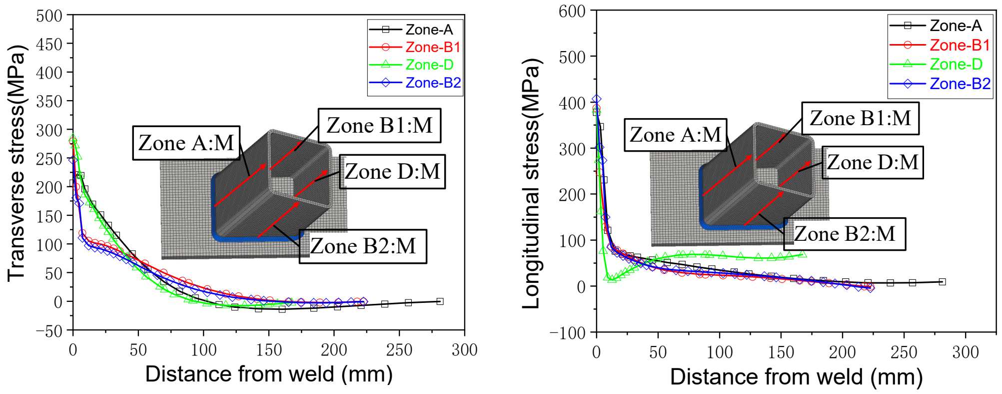

(**a**) (**b**)

Figure 11. Residual stress distribution in the branch pipes of the joint considering phase transformation effects: (**a**) Transverse; (**b**) Longitudinal.

5.2. The Effects of Different Welding Sequences on Joint Residual Stresses and Microstructure

To further investigate the effects of different welding sequences on the residual stresses in the branch pipes of joints, three welding sequences were employed to numerically simulate the welding process. The welding sequences are presented in Table 5, where WS-1 involves the clockwise welding of the four regions, repeated three times; WS-2 consists of the symmetrical welding of the four regions, repeated three times; and WS-3 involves the symmetrical welding of each region, with three passes completed in one region before moving on to the next. Figure 12 illustrates the peak welding residual stresses on the surface of the branch pipes in various regions along path "M" under the three welding sequences. The numerical simulation results show that the relative errors of the peak transverse and longitudinal residual stresses in the branch pipes near the weld were within 5% for the three welding sequences. This indicates that there were no significant differences in the peak welding residual stresses among the various regions of the joint under three welding sequences.

Table 5. Three joint welding sequences.

WS-1	WS-2	WS-3
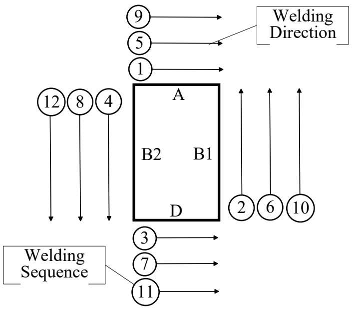	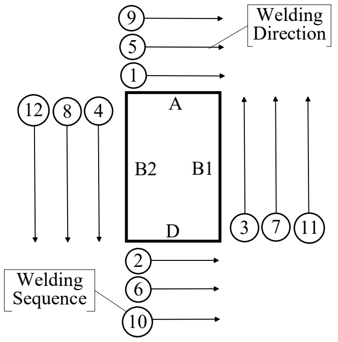	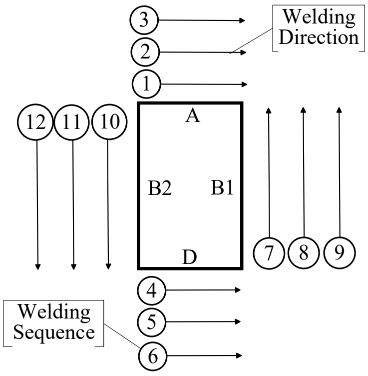

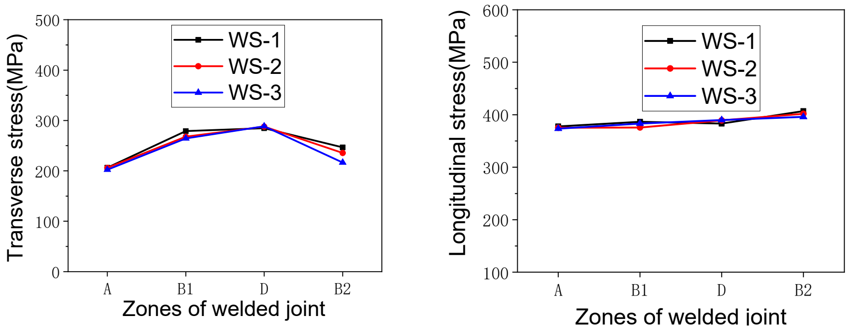

(**a**) (**b**)

Figure 12. Peak residual stresses in the branch pipes of different joint regions under three welding sequences: (**a**) Transverse; (**b**) Longitudinal.

Figures 13 and 14, respectively, show the T8/5 cooling rates and microstructural compositions for different weld passes across various regions of the joint. In Figure 14, B represents bainite, P represents pearlite, M represents martensite, and F represents ferrite. Figures 13a and 14a show, respectively, the T8/5 cooling rates and microstructure contents for the first weld pass (WP-1) in the four weld zones of the joint. It is evident that the T8/5 cooling rates and microstructure contents exhibit a consistent trend across the three welding sequences. The contents of ferrite, martensite, pearlite, and bainite in regions A, B1, and B2 are 0.65, 0.15, 0.03, and 0.17, respectively, while in region D, the contents are 0.48, 0.40, 0.02, and 0.10, respectively. The weld in Zone D has a higher T8/5 cooling rate, resulting in a microstructure with a higher martensite content, whereas the other zones have lower T8/5 cooling rates, with the microstructure predominantly composed of ferrite.

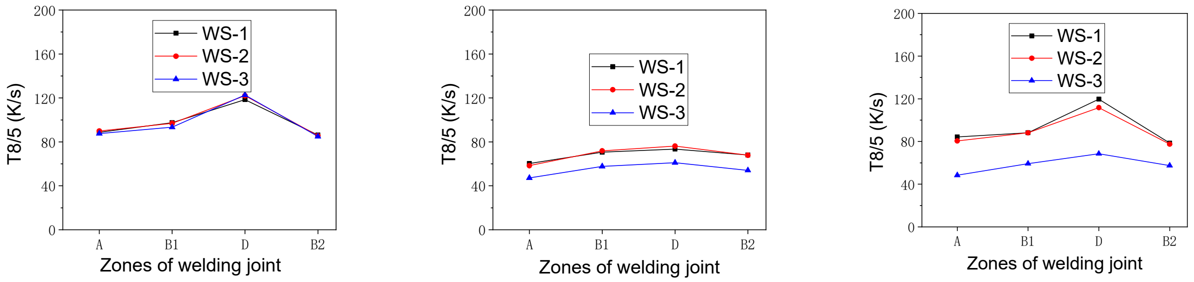

(**a**) (**b**) (**c**)

Figure 13. T8/5 cooling rates in different weld passes: (**a**) WP-1; (**b**) WP-2; (**c**) WP-3.

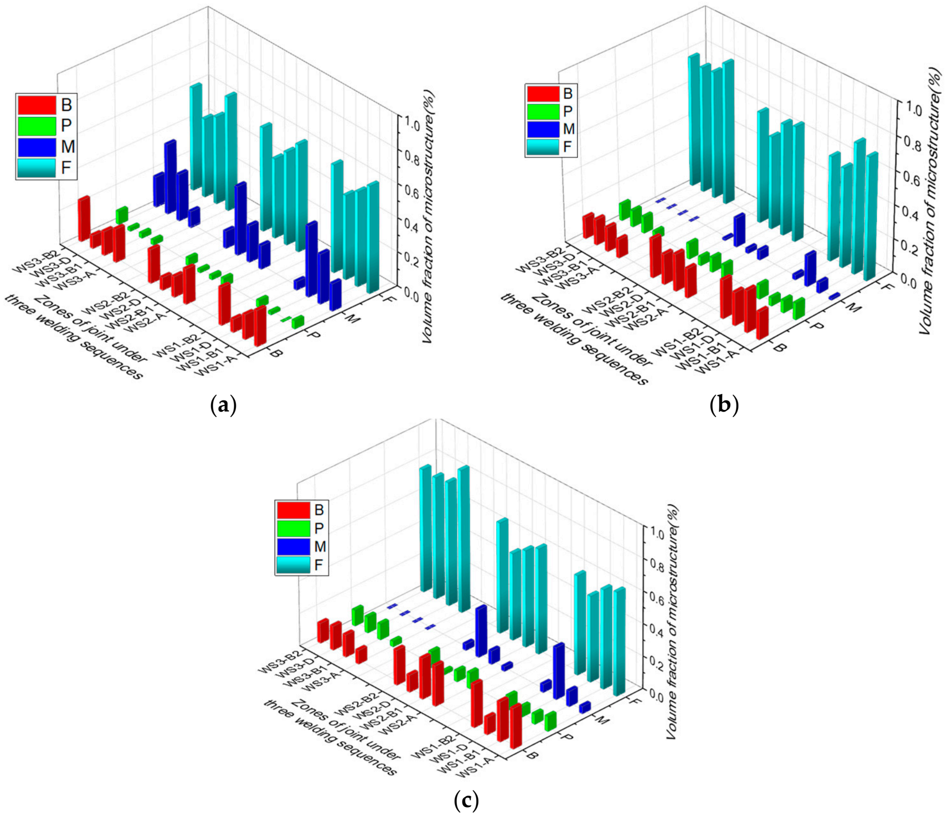

(**a**) (**b**)

(**c**)

Figure 14. Microstructure contents in different weld passes: (**a**) WP-1; (**b**) WP-2; (**c**) WP-3.

Figures 13b and 14b showcase the T8/5 cooling rates and microstructural compositions of the second weld pass (WP-2) in the four weld zones, respectively. The contents of ferrite, martensite, pearlite, and bainite in regions A, B1, and B2 for welding sequences WS-1 and WS-2 are 0.66, 0.05, 0.14, and 0.15, respectively, while in region D, the contents are 0.59, 0.18, 0.06, and 0.17, respectively. For welding sequence WS-3, the contents of ferrite, martensite, pearlite, and bainite in regions A, B1, B2, and D are 0.71, 0.02, 0.10, and 0.17, respectively. Notably, the T8/5 cooling rate under the WS-3 welding sequence is lower than that under the WS-1 and WS-2 sequences, resulting in a lower martensite content in the WS-3 sequence compared with WS-1 and WS-2.

Figures 13c and 14c, respectively, present the T8/5 cooling rates and microstructural compositions of the third weld pass (WP-3) in the four zones. The contents of ferrite, martensite, pearlite, and bainite in regions A, B1, and B2 for welding sequences WS-1 and WS-2 are 0.62, 0.08, 0.09, and 0.21, respectively, while in region D, the contents are 0.54, 0.25, 0.08, and 0.13, respectively. For welding sequence WS-3, the contents of ferrite, martensite, pearlite, and bainite in regions A, B1, B2, and D are 0.76, 0.00, 0.10, and 0.14, respectively. A significant reduction in the T8/5 cooling rate under the WS-3 welding sequence compared with WS-1 and WS-2 is observed, leading to a lower martensite content in the WS-3 sequence.

Overall, under the WS-1 and WS-2 welding sequences, the higher T8/5 cooling rates result in a microstructure containing a small amount of martensite in the weld zones, particularly in the D zone, where the martensite content ranges from 18% to 40%. Conversely, under the WS-3 welding sequence, the lower T8/5 cooling rates lead to a microstructure with less martensite in the weld zones.

6. Summary

This study investigated the effects of phase transformation and welding sequences on the welding residual stress distributions in a square tube–plate Y-shaped joint through numerical simulation. The following conclusions were drawn based on the findings of this study:

(1) On the outer surface of the branch pipe of the joint, both the transverse and longitudinal residual stresses were tensile stresses along path "M" near the weld. The peak value of the longitudinal residual stress is higher than that of the transverse residual stress and exceeds the yield strength of the base material of the branch pipe.

(2) The peak transverse residual stress calculated using the phase transformation effect was lower than that calculated without considering the phase transformation effect. Along path "M", the peak transverse residual stresses in regions A, B1, B2, and D decreased by 17.41%, 25.81%, 9.45%, and 8.13%, respectively.

(3) Three welding sequences, WS-1, WS-2, and WS-3, were employed to weld the joints. Under the welding sequences, no significant differences were observed in the peak transverse and longitudinal residual stresses near the weld on the branch pipe surface.

(4) Under the three welding sequences, the microstructures in various regions of the first weld pass of the joint remained essentially consistent. Region D is mainly composed of martensite and ferrite, while the microstructures of the welds in the other regions are predominantly ferrite. In the WS-3 welding sequence, the microstructures in all regions of the second and third weld passes of the joint are primarily ferrite, with almost no martensite content. However, under the WS-1 and WS-2 welding sequences, the microstructures in all regions of the second and third welds are mainly ferrite but contain a certain amount of martensite, especially in region D, where the martensite content ranges from 18% to 40%.

Author Contributions: Software, Z.Y.; Investigation, Z.Y.; Resources, J.J.; Supervision, J.J. All authors have read and agreed to the published version of the manuscript.

Funding: This research received no external funding.

Data Availability Statement: The original contributions presented in this study are included in the article. Further inquiries can be directed to the corresponding author.

Conflicts of Interest: The authors declare no conflict of interest.

References

1. Jiang, J.; Lee, C.K.; Chiew, S.P. Residual stress and stress concentration effect of high strength steel built-up box T-joints. *J. Constr. Steel Res.* **2015**, *105*, 164–173. [CrossRef]
2. Lu, Y.; Lu, C.; Zhang, D.; Chen, T.; Zeng, J.; Wu, P. Numerical computation methods of welding deformation and their application in bogie frame for high-speed trains. *J. Manuf. Process* **2019**, *38*, 204–213. [CrossRef]
3. Brar, G.S.; Singh, C.S. FEA of residual stress in cruciform welded joint of hollow sectional tubes. *J. Constr. Steel Res.* **2014**, *102*, 44–58. [CrossRef]
4. Sepe, R.; Wiebesiek, J.; Sonsino, C.M. Numerical and experimental validation of residual stresses of laser-welded joints and their influence on the fatigue behavior. *Fatigue Fract. Eng. Mater. Struct.* **2020**, *43*, 1126–1141. [CrossRef]
5. Cui, C.; Zhang, Q.; Bao, Y.; Bu, Y.; Luo, Y. Fatigue life evaluation of welded joints in steel bridge considering residual stress. *J. Constr. Steel Res.* **2019**, *153*, 509–518. [CrossRef]
6. Hensel, J.; Nitschke-Pagel, T.; Ngoula, D.T.; Beier, H.-T.; Tchuindjang, D.; Zerbst, U. Welding residual stresses as needed for the prediction of fatigue crack propagation and fatigue strength. *Eng. Fract. Mech.* **2018**, *198*, 123–141. [CrossRef]

7. Goldak, J.A.; Akhlaghi, M. *Computational Welding Mechanics*; Springer: New York, NY, USA, 2005.
8. Cui, S.; Pang, S.; Pang, D.; Zhang, Q.; Zhang, Z. Numerical Simulation and Experimental Investigation on 2205 Duplex Stainless Steel K-TIG Welded Joint. *Metals* **2021**, *11*, 1323. [CrossRef]
9. Guo, X.K. Inversing Parameter Values of Double Ellipsoid Source Model During Multiple Wires Submerged Arc Welding by Using Pattern Search Method. Master's Thesis, Shanghai Jiao Tong University, Shanghai, China, 2009.
10. Jia, X.; Xu, J.; Liu, Z.; Huang, S.; Fan, S.; Sun, Z. A new method to estimate heat source parameters in gas metal arc welding simulation process. *Fusion Eng. Des.* **2014**, *89*, 40–48. [CrossRef]
11. Zhang, H.W.; Gui, L.J.; Fan, Z.J. Research and verification of welding heat source parameters optimization model. *J. Tsinghua Univ. (Sci. Technol.)* **2022**, *52*, 367–373.
12. Wang, J.; Wang, J.; Zhao, Y.; Li, Y.; Zhan, X. Microstructure, Thermal Behavior and Tensile Properties of Laser Welded Bottom-Locking Joint for TA15 Titanium Alloy. *Met. Mater. Int.* **2023**, *29*, 1441–1453. [CrossRef]
13. Cui, S.; Pang, S.; Pang, D.; Zhang, Z. Influence of welding speeds on the morphology, mechanical properties, and microstructure of 2205 DSS welded joint by K-TIG welding. *Materials* **2021**, *14*, 3426. [CrossRef]
14. Ji, W.; Zhang, P.; Luo, K. Investigation of welding temperature field and residual stresses of corrugated steel web girders. *Structures* **2022**, *44*, 1416–1428. [CrossRef]
15. Cheon, J.; Na, S.-J. Influence of simulation methods of temperature distribution on thermal and metallurgical characteristics in GMA welding. *Mater. Des.* **2016**, *108*, 183–194. [CrossRef]
16. Zhang, Y.L.; Liu, X.C.; Zhou, Y.; Shi, Y.L. Influence of welding method on residual stress and metallography of a mild steel welded butt-joint plate. *J. Constr. Steel Res.* **2022**, *199*, 107640. [CrossRef]
17. Malik, A.M.; Qureshi, E.M.; Dar, N.U.; Khan, I. Analysis of circumferentially arc welded thin-walled cylinders to investigate the residual stress fields. *Thin-Walled Struct.* **2008**, *46*, 1391–1401. [CrossRef]
18. Joshi, S.; Semetay, C.; Price, J.W.; Nied, H.F. Weld-induced residual stresses in a prototype dragline cluster and comparison with design codes. *Thin-Walled Struct.* **2010**, *48*, 89–102. [CrossRef]
19. Hemmesi, K.; Farajian, M.; Siegele, D. Numerical and experimental description of the welding residual stress field in tubular joints for fatigue assessment. *Weld. World* **2016**, *60*, 741–748. [CrossRef]
20. Gadallah, R.; Tsutsumi, S.; Tanaka, S.; Osawa, N. Accurate evaluation of fracture parameters for a surface-cracked tubular T-joint taking welding residual stress into account. *Mar. Struct.* **2020**, *71*, 102733. [CrossRef]
21. Jin, D.; Hou, C.; Shen, L. Effect of welding residual stress on the performance of CFST tubular joints. *J. Constr. Steel Res.* **2021**, *184*, 106827. [CrossRef]
22. Wang, Y.; Feng, G.; Pu, X.; Deng, D. Influence of welding sequence on residual stress distribution and deformation in Q345 steel H-section butt-welded joint. *J. Mater. Res. Technol.* **2021**, *13*, 144–153. [CrossRef]
23. Zhang, H.; Ouyang, Z.; Li, L.; Ma, W.; Liu, Y.; Chen, F.; Xiao, X. Numerical study on welding residual stress distribution of corrugated steel webs. *Metals* **2022**, *12*, 1831. [CrossRef]
24. He, Z.; Huang, B.; Chen, L.; Zheng, J.; Yang, J.; Wang, S. Effect of Groove Angle on Stress Field and Deformation of Q345/316 Dissimilar Metal Welded Joints. *J. Mater. Eng. Perform.* **2022**, *31*, 6891–6903. [CrossRef]
25. Akduman, S.; Karalar, M.; Mert, N.; Öztürk, H. Investigation of the Post-Fire Behavior of Different End-Plated Beam–Column Connections. *Buildings* **2024**, *14*, 1013. [CrossRef]
26. Martin, J.W.; Doherty, R.D.; Cantor, B. *Stability of Microstructure in Metallic Systems*; Cambridge University Press: Cambridge, UK, 1997.
27. Xavier, C.R.; Delgado Junior, H.G.; Castro JA, D.; Ferreira, A.F. Numerical pre-dictions for the thermal history, microstructure and hardness distributions at the HAZ during welding of low alloy steels. *Mater. Res.* **2016**, *19*, 520–533. [CrossRef]
28. Zhang, Q.; Xie, J.; Gao, Z.; London, T.; Griffiths, D.; Oancea, V. A metallurgical phase transformation framework applied to SLM additive manufacturing processes. *Mater. Des.* **2019**, *166*, 107618. [CrossRef]
29. Eshraghi-Kakhki, M.; Kermanpur, A.; Golozar, M.A. Threedimensional simulation of quenching process of plain carbon steel gears incorporating phase transformations. *Mater. Sci. Technol.* **2012**, *28*, 197–204. [CrossRef]
30. Ronda, J.; Oliver, G.J. Consistent thermo-mechano-metallurgical model of welded steel with unified approach to derivation of phase evolution laws and transformation-induced plasticity. *Comput. Meth. Appl. Mech. Eng.* **2000**, *189*, 361–418. [CrossRef]
31. Deng, D.A.; Murakawa, H. Finite element analysis of temperature field, microstructure and residual stress in multi-pass butt-welded 2.25Cr-1Mo steel pipes. *Comput. Mater. Sci.* **2008**, *43*, 681–695. [CrossRef]
32. Hu, L.; Wang, Y.; Li, S.; Zhang, C.; Deng, D. Study on Computational Prediction About Microstructure and Hardness of Q345 Steel Welded Joint Based on SH-CCT Diagram. *Acta Metall. Sin.* **2021**, *57*, 1073–1086.
33. Li, Y.; Hou, J.-Y.; Zheng, W.-J.; Wan, Z.-Q.; Tang, W.-Y. A Numerical Simulation Method Considering Solid Phase Transformation and the Experimental Verification of Ti6Al4V Titanium Alloy Sheet Welding Processes. *Materials* **2022**, *15*, 2882. [CrossRef]
34. Esfahani, A.K.; Babaei, M.; Sarrami-Foroushani, S. A numerical model coupling phase transformation to predict microstructure evolution and residual stress during quenching of 1045 steel. *Math. Comput. Simul.* **2021**, *179*, 1–22. [CrossRef]
35. Wei, X.; Zhang, X.; He, W.; Li, J.; Zhang, J.; Li, D.; Li, S. Influence of Deep Cryogenic Treatment on Microstructural Evolution and Transformation Kinetics Simulation by Finite Element Method of Low-Carbon High-Alloy Martensitic-Bearing Steel. *Steel Res. Int.* **2022**, *93*, 2100785. [CrossRef]

36. Sun, B.; Liu, H.; Tang, J.; Rong, S.; Liu, Y.; Jiang, W. Optimization of heat treatment deformation control process parameters for face-hobbed hypoid gear using FEA-PSO-BP method. *J. Manuf. Process.* **2024**, *117*, 40–58. [CrossRef]
37. Saunders, N.; Guo, Z.; Li, X.; Miodownik, A.P.; Schille, J.-P. *The Calculation of TTT and CCT Diagrams for General Steels*; Sente Software Ltd.: Guildford, UK, 2004.
38. Islam, M.; Buijk, A.; Rais-Rohani, M.; Motoyama, K. Simulation-based numerical optimization of arc welding process for reduced distortion in welded structures. *Finite Elem. Anal. Des.* **2014**, *84*, 54–64. [CrossRef]
39. Şimşir, C.; Gür, C.H. 3D FEM simulation of steel quenching and investigation of the effect of asymmetric geometry on residual stress distribution. *J. Mater. Process. Technol.* **2008**, *207*, 211–221. [CrossRef]